JOURNAL OF SPACECRAFT AND ROCKETS
Vol. 45, No. 6, November–December 2008

Stage-Separation Aerodynamics of Two-Stage Space Transport Systems Part 2: Unsteady Simulation

Mochammad A. Moelyadi,* Christian Breitsamter,† and Boris Laschka‡
Technische Universität München, 85747 Garching, Germany

DOI: 10.2514/1.35059

The separation maneuver, one of the critical phases of the two-stage-to-orbit ascent flight mission, causes the changes of the position and intensity of shock waves and the points of interaction of reflected shock waves, which provide strong unsteady airloads on the orbital and carrier stages. The time-dependent simulation of the stage separation is performed by considering the effects of unsteady flows due to the orbital motion from the beginning separation to a position at which the interaction between the stages vanishes. The orbital-stage motion is approached using harmonic motions simultaneously in the orbital-stage angle of attack and the separation distance stated in the one-minus-cosine function. The unsteady-flow solution is obtained by solving Euler equations using a dual-time-stepping methodology. This method employs a pseudotime to redefine the unsteady-flow problem into a steady-flow problem, with the physical time derivative included in the discretized equations. The meshes change on the flow domain for each time step following the orbital motion, which are generated by applying the concept of a dynamic grid. The results substantiate that unsteady characteristics must be carefully considered in the beginning of the separation maneuver when there is a significant decrease in orbital-stage lift along with a strong change in pitching moment.

Nomenclature

C_D	=	total drag coefficient
C_L	=	total lift coefficient
C_M	=	total pitching-moment coefficient
h	=	relative distance
k_{red}	=	reduced frequency
l_{EOS}	=	reference length of elliptical aerodynamic configuration orbital stage
M_∞	=	freestream Mach number
$\mathbf{Q}$	=	state variables in curvilinear and dimensionless coordinate system
$\mathbf{R}$	=	residual
t	=	real physical time
t^*	=	pseudotime
V_∞	=	freestream velocity
$\Delta\alpha$	=	relative angle of attack
ρ	=	density
τ	=	time in curvilinear coordinates
Ω	=	control volume
ω	=	angular velocity

I. Introduction

TO GUARANTEE a safe separation of two-stage space transportation systems, investigations on the unsteady aerodynamics of the fully two-stage-to-orbit (TSTO) vehicle are required: namely, to describe flow behaviors of stage separation and to determine amplitude and phase of aerodynamic forces and moments. As shown in Fig. 1, the separation maneuver will be one of the critical phases of the ascent flight mission for the vehicle system, occurring at the speed flight of approximately Mach of 6.8 and the altitude of 35 km [1]. In such a phase, the space vehicle system is subject to very high dynamic pressures. Under these conditions, aerodynamic interferences occur between the stages: namely, complex interactions of incident and reflected shock waves and expansion waves with each other as well as with boundary layers. Furthermore, the separation process influences the position and intensity of the shock waves and the points of interaction of the reflected shock waves that provide strong unsteady airloads on both stages. This may have an impact on the stability of the vehicle during the separation maneuver, causing a hazard during the space vehicle operation.

The problems of two-stage space transport systems during a separation maneuver have been investigated in numerous experimental and numerical studies. In the 1960s, Decker [2] performed an analysis of the aerodynamic performance and the aerodynamic interference effects of the parallel-staged simple configurations at Mach numbers 3 and 6 during separation, and the aerodynamic data obtained constitute the input for the system of equations of dynamic motion. During the space shuttle program in the 1970s, several measurements and calculations dealing with the separation of the liquid-fuel tank from the shuttle orbiter were accomplished [3]. In addition, the experimental studies in [4,5] deal with separation of two winged stages, accomplished in the mid-1990s. These results extended the knowledge on such classes of complicated flows and are necessary for testing the numerical methods developed. The recent experimental measurements on the separation of two-stage space transport systems were carried out with the full configuration of the carrier and orbital stages [6,7]. These experiments provide a database of aerodynamic characteristics of separating models of the orbital and carrier stages, including their interferences.

Moreover, in the period between 1985 and 1990, there was a significant increase in the application of computational fluid dynamics for modeling hypersonic flows. For example, a method for calculating aerodynamic characteristics of the first stage (fuel tank) and the orbital stage (Buran vehicle) during separation is proposed in [8]. The flowfield in the vicinity of the first stage is calculated using the McCormack scheme and is used to calculate the characteristics of the second stage. The other examples are the computations of several flight situations of the ascent flight, including the separation maneuver. These were performed using the three-dimensional Euler and three-dimensional Navier–Stokes methods [9–11]. However, all

Received 9 October 2007; revision received 20 June 2008; accepted for publication 7 July 2008.

*Research Engineer, Institute of Aerodynamics; moelyadi1968@hotmail.com.
†Chief Scientist, Institute of Aerodynamics; Christian.Breitsamter@aer.mw.tum.de. Associate Fellow AIAA.
‡Professor Emeritus, Institute of Aerodynamics; Laschka@aer.mw.tum.de. Honorary Fellow AIAA.

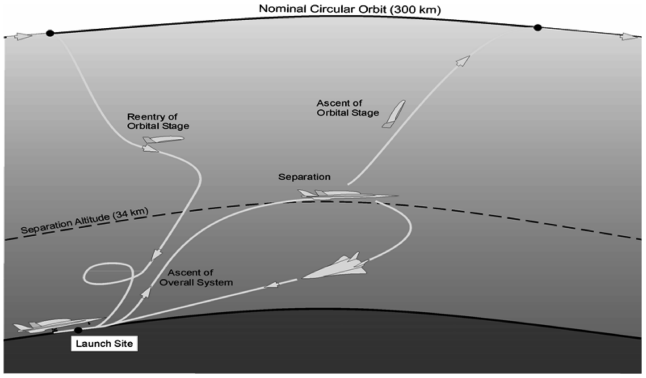

Fig. 1 Flight mission of the two-stage space transportation system.

preceding investigations assume a steady flowfield and thus neglect additional velocities induced from separation maneuver. Based on the results in [12], Meakin and Suhs [13] showed that the effects of unsteady flows during separation due to the shock interactions between the upper stage and lower stage are nonnegligible. This indication is also supported by Cvrlje et al. [14], who performed numerical simulation involving both roll and yaw oscillations of an orbital vehicle for different reduced frequencies. They also presented the effects of unsteady flows, including laminar boundary layers on the longitudinal motions of an idealized two-stage hypersonic vehicle during separation [15]. Although the phenomena of unsteady flows on the two-stage space vehicle have a significant effect on safety during a separation maneuver, few investigations exist for unsteady cases as presented in [1,10,14,16]. The investigations have been accomplished for incomplete geometries and simple trajectories of the separation maneuver. This is due to the difficulty of generating proper meshes in the physical domain around the complex geometry model. Also, the complex geometry will produce more complex flow behavior in the flowfield. Therefore, when investigating unsteady flows for the complex configuration, it is challenging to make a realistic simulation of the unsteady flow of two-stage space transport systems during the separation maneuver.

This paper presents the investigation of the unsteady flowfield and aerodynamic characteristics for a two-stage space transport system during separation based on computational fluid dynamics. Unsteady-flow computations are performed by considering time-dependent flows generated by the orbital-stage motion during separation. The important unsteady-flowfield parameters such as reduced frequency and amplitude of rotation and translation are studied.

The unsteady-flow simulation is carried out by solving unsteady Euler equations using a dual-time-stepping methodology. The deformation of mesh on the flow domain for each time step is generated by applying the concept of a dynamic grid. Such a deformation of mesh follows the orbital motion in which the path is modeled as a harmonic motion simultaneously in the orbital-stage angle of attack and separation distance stated in the one-minus-cosine function.

II. Computational Simulations of Stage Separation

A. Numerical Method for the Unsteady-Flow Solution

Based on the finite volume approach, the unsteady Euler equation can be written as a system of coupled ordinary differential equations in time for all control volumes $\Omega_{i,j,k}$, as follows:

$$\frac{\mathrm{d}(\Omega\mathbf{Q})_I}{\mathrm{d}t} = -\mathbf{R}_I \tag{1}$$

where $\mathbf{R}$ is the residual, and the index I denotes the particular control volume. The residual is a nonlinear function of the conservative variable $\mathbf{Q}$. This equation system has to be integrated in time, either to obtain a steady-state solution ($\mathbf{R}_I = 0$) for an initial input of the unsteady computation or to reproduce the time history of an unsteady flow. The solutions of the unsteady flow are performed by employing the dual-time-stepping methodology proposed by Jameson [17]. Such a method redefines the unsteady-flow problem into a steady-flow problem by introducing a pseudotime, with the physical time derivative included in the discretized equation. The dual-time-stepping approach is second-order in time and is written as

$$\frac{3(\Omega)_I^{n+1}\mathbf{Q}_I^{n+1} - 4(\Omega)_I^{n}\mathbf{Q}_I^{n} + (\Omega)_I^{n-1}\mathbf{Q}_I^{n-1}}{2\Delta t} = -\mathbf{R}_I^{n+1} \tag{2}$$

where Δt denotes the global physical time step. Equation (2) employs a 3-point backward-difference approximation of the time derivative in Eq. (1). For the numerical calculation, this equation is approximated by introducing a pseudotime variable t^* and can be written as

$$\frac{\mathrm{d}}{\mathrm{d}t^*}(\Omega_I^{n+1}\mathbf{Q}_I^*) = -\mathbf{R}_I^*(\mathbf{Q}_I^*) \tag{3}$$

where $\mathbf{Q}^*$ is the approximation of Q^{n+1}. The unsteady residual is defined as

$$\mathbf{R}_I^*(\mathbf{Q}_I^*) = \mathbf{R}_I(\mathbf{Q}_I^*) + \frac{3}{2\Delta t}(\Omega_I^{n+1})\mathbf{Q}_I^* - S_I^* \tag{4}$$

where Ω^{n+1} is a new size of control volume that changes and has to satisfy the geometry conservation law. This is intended to avoid errors induced by the deformation of the control volumes [18]. The geometry conservation law is automatically satisfied for such moving grids, in which the shape of the control volume does not change in time. In addition, the source term on the right-hand side of Eq. (4), gathering all constant values during the time-stepping, is written as

$$S_I^* = \frac{2}{\Delta t}(\Omega)_I^n\mathbf{Q}_I^n - \frac{1}{2\Delta t}(\Omega)_I^{n-1}\mathbf{Q}_I^{n-1} \tag{5}$$

To solve the pseudoproblem in Eq. (3), the explicit multistage Runge–Kutta scheme [19] is used by employing the pseudotime step t^* and the new size of the control volume Ω^{n+1}. The time-marching process is started with the values of the steady solution. Then it is continued until the values of the conservative variable at the new pseudotime level (Q_I^*) approximates the conservative value at $t + \Delta t(\mathbf{Q}_I^{n+1})$ with sufficient accuracy (i.e., when the residual $\mathbf{R}_I^*$ reduces by 3 orders of magnitude).

B. Dynamic Grids

To carry out unsteady calculations that involve a moving solid surface, a dynamic adaptation of mesh to the actual body position must be performed for each time step in the computational domain. This assumes that the edges of the outer boundaries remain unchanged and only the configuration itself is moved. According to that, the grid must be adjusted and distorted by the movement of the solid body and the fixed outer boundaries. Moreover, it must be guaranteed that the quality of the computational grid remains good during this deformation.

For the simulation of the stage separation of the TSTO space transportation vehicle, the computational domain for the moving grids is limited in given regions around the elliptical aerodynamic configuration (ELAC) orbital-stage (EOS) model that was generated with the O-grid topology, as shown in Fig. 2. The inner boundary of the mesh at which the solid surface resides has to conform to the motion of the EOS surface at all times. The mesh outer boundary of the O-grid is free to move or is fixed. The velocity of the mesh, as well as the deformation of the cells, is considered in the unsteady transformation of the Euler equations.

The good quality of the computational grid is obtained by locally smoothing the mesh by solving the Laplace equations.

C. Model of the Separation Path of the Orbital Stage

The model of the separation path of the orbital stage is taken from the flight mechanics analysis data for the TSTO space transport system, as shown in Fig. 3 [20]. The separation process takes place with the orbital stage relatively moving simultaneously in the separation distance and orbital-stage angle of attack. The graphs of

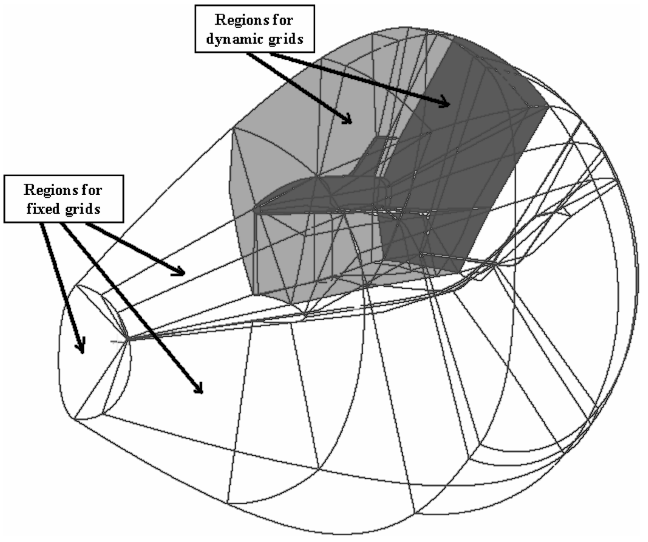

Fig. 2 Computational domain for dynamic grids.

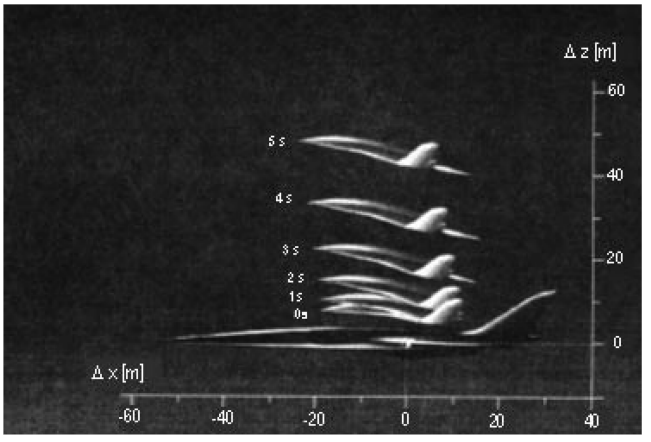

Fig. 3 Trajectory of stage separation of TSTO space vehicle system.

the relative angle of attack $\Delta\alpha$ and relative distance h/l_{EOS} against time are given in Fig. 4.

To perform the computational simulations of the stage separation, the staging path is approached with a harmonic function: namely, a one-minus-cosine function is applied for the relative angle of attack and relative distance, as follows:

$$\Delta\alpha(\tau) = \Delta\alpha_0 + \frac{(\Delta\alpha_1 - \Delta\alpha_0)}{2}(1 - \cos(k\tau)) \tag{6}$$

$$h(\tau) = h_0 + \frac{(h_1 - h_0)}{2}(1 - \cos(k\tau)) \tag{7}$$

where α_0, h_0, α_1, and h_1 are constants of the orbital-stage angle of attack and separation distance at the initial position and the end position of the separation process, respectively, and τ is the time step. The reduced frequency k_{red} constitutes a number expressing a ratio of the angular velocity to the freestream velocity. Increasing the reduced frequency provides the higher angular velocity; hence, the effects of time-dependent flows due to the orbital-stage motion become greater. The nondimensional time-step size τ and reduced frequency k_{red} for unsteady flow are written as [21]

$$\tau = \frac{V_\infty}{l_{\text{EOS}}} t \tag{8}$$

$$k_{\text{red}} = \frac{l_{\text{EOS}}}{V_\infty} \omega \tag{9}$$

III. Analysis of the Unsteady Aerodynamics of a TSTO Separation Maneuver

The computations of the unsteady aerodynamics of the stage separation are performed on the full two-stage-to-orbit configurations (EOS and ELAC). The simulation of the stage-separation models the orbital stage discarding from an initial position above (close to the carrier stage) to a position at which the interaction between the stages vanishes. Previously, to reach the initial position of the separation, the orbital stage was lifted up using a strut mechanism from the basin of the carrier stage. The motion of the orbital stage may result in time-dependent flows, including a downwash, and changes of the flow properties in the gap region between the stages. At the beginning separation, the orbital stage may perform a pause (zero velocity of the orbital stage relative to the carrier stage) before continuing the separation or it may continuous move itself up to go along a given trajectory. For the first condition, there is no time-dependent flow occurring at the beginning separation. Moreover, for the second condition, the orbital motion produces fully time-dependent flows at the beginning separation. For the latter case, it is necessary to model the orbital motion as a harmonic motion by applying for a one-minus-cosine function in both relative angle of attack and distance, as written in Eqs. (6) and (7), respectively. In addition, the simulation only simulates a part of the stage separation, with the beginning position using the value of the orbital-stage angle of attack lower than that of the proposed flight mechanics data, as shown in Fig. 4. The initial position is set in the orbital-stage angle of attack, $\Delta\alpha$ of 2.0 deg, and the separation distance between the stages, $\mathbf{h}/\mathbf{l}_{\text{EOS}}$, is equal to 0.125. Moreover, the end position of the orbital stage is $\Delta\alpha = 6.0$ deg and

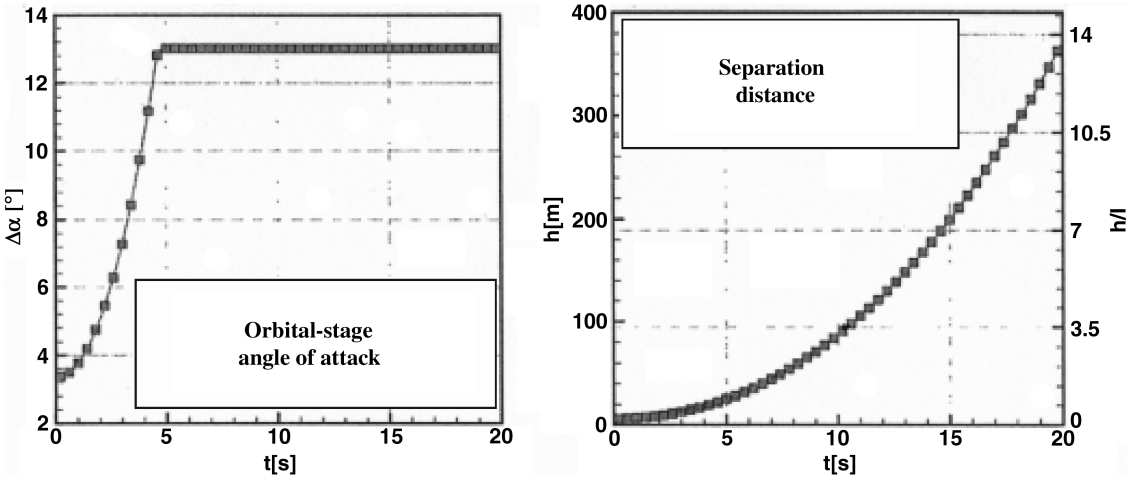

Fig. 4 Parameters of stage separation of the TSTO space vehicle system.

$\mathbf{h}/\mathbf{l}_{\mathrm{EOS}} = 0.325$. The pitching reference point of the orbital motion is $x/l_{\mathrm{EOS}} = 0.65$ with respect to the nose of the EOS stage.

Furthermore, the unsteady-flow calculation requires the steady-flow solution as an initial input. Then it is run for the number of time steps per cycle. The solution of each time step depends on the position of the orbital stage. In this paper, one cycle of the computation consists of 40 time steps: that is, from the initial position and back to the initial position again. The convergence solution for each time step results if the residual of relative density does not exceed 5×10^{-4}. In addition, the simulations are performed for three different reduced frequencies (including, namely, $k_{\mathrm{red}} = 0.22$, 0.5, and 1.0) using the same initial state. Figure 5 shows the results of six different amplitudes of the dynamic grids. The mesh deformation occurs only in limited regions around the EOS model that was generated with the O-grid topology. The mesh close to the solid surface conforms to the motion of the EOS surface at all times. The remaining meshes outside the moving regions remain fixed.

A. Aerodynamic Characteristics of Unsteady Stage Separation

Figures 6–8 show the result of aerodynamic characteristics (including lift, drag, and pitching-moment coefficients) for one-and-a-half cycles at a freestream Mach number of 4.04 and reduced frequencies of 0.22, 0.5, and 1.0, respectively. The results of the lift coefficient at the steady-state condition are also presented in the figures. There are discrepancies in aerodynamic-characteristic results between the first half- and the second half-cycles: in particular, in the lift coefficient. For the first cycle, the lift coefficient at the beginning separation has the same value as the corresponding steady-flow solution. This is related to the case in which the orbital

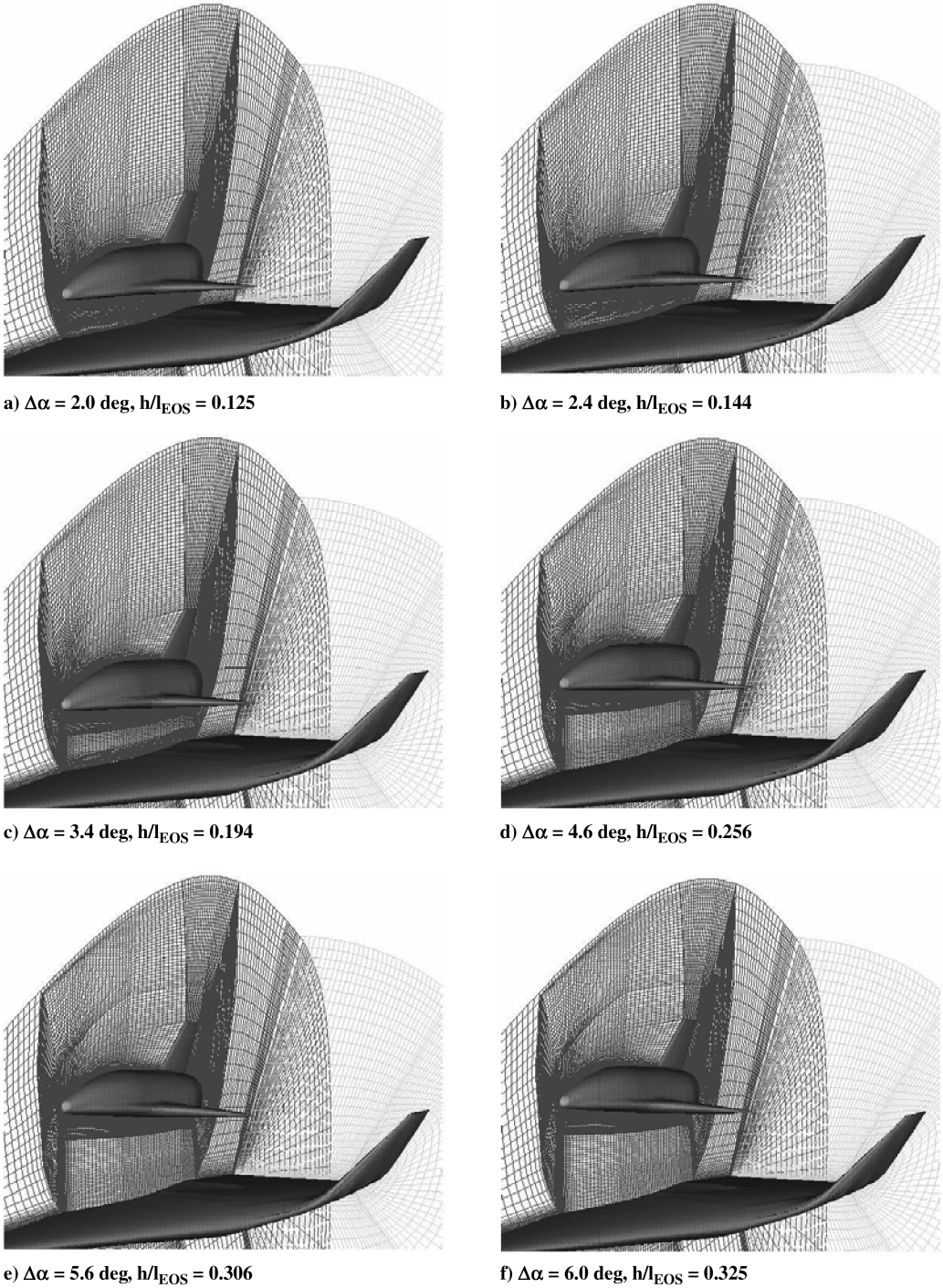

a) $\Delta\alpha$ = 2.0 deg, h/l$_{\mathrm{EOS}}$ = 0.125

b) $\Delta\alpha$ = 2.4 deg, h/l$_{\mathrm{EOS}}$ = 0.144

c) $\Delta\alpha$ = 3.4 deg, h/l$_{\mathrm{EOS}}$ = 0.194

d) $\Delta\alpha$ = 4.6 deg, h/l$_{\mathrm{EOS}}$ = 0.256

e) $\Delta\alpha$ = 5.6 deg, h/l$_{\mathrm{EOS}}$ = 0.306

f) $\Delta\alpha$ = 6.0 deg, h/l$_{\mathrm{EOS}}$ = 0.325

Fig. 5 Dynamic mesh of the EOS and ELAC vehicle for various $\Delta\alpha$ and h/l_{EOS}.

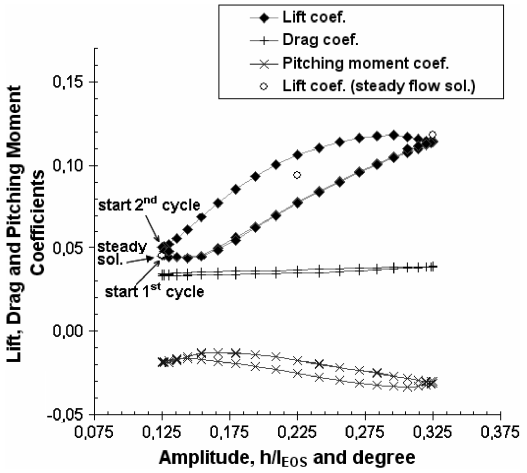

Fig. 6 Aerodynamic characteristics of unsteady stage separation for the reduced frequency of $k_{red} = 0.22$.

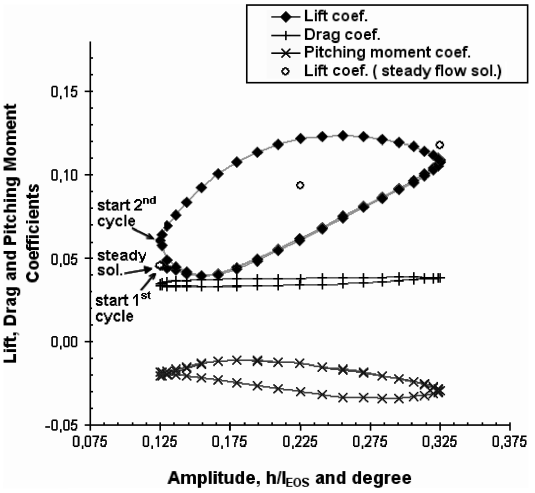

Fig. 7 Aerodynamic characteristics of unsteady stage separation for the reduced frequency of $k_{red} = 0.50$.

stage performs a pause at the beginning separation. The second cycle results exhibit the continuous motion of the orbital stage at the beginning separation, in which time-dependent flows are considered. This affects an additional lift on the orbital stage, which increases with increasing the reduced frequency, as shown in Figs. 7 and 8. This is due to the higher reduced frequency, indicating that the higher velocity of the orbital stage relative to the carrier stage produces the larger unsteady-flow effect.

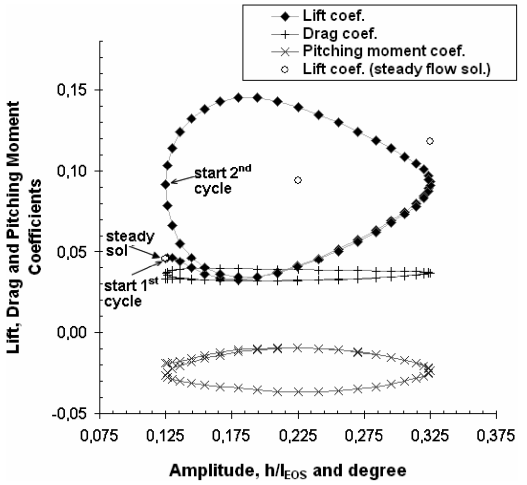

Fig. 8 Aerodynamic characteristics of unsteady stage separation for the reduced frequency of $k_{red} = 1.0$.

The computation at each reduced frequency obtains the different profiles of unsteady aerodynamic coefficients. At the lower reduced frequency (as shown in Fig. 6, for example), the effect of the unsteady flow contributes only to a small additional lift of the orbital stage. Increasing the amplitude of the stage separation provides an increase of the EOS lift coefficient, but at the beginning of the separation, the lift coefficient slightly decreases. At the higher reduced frequency, the effect of the unsteady flow has great influence on the orbital-stage lift coefficient. The orbital stage experiences a large decrease in lift coefficient with increasing the amplitude until the minimum lift coefficient is reached. Further, an increase of the amplitude causes a higher increase of the lift coefficient of the EOS. In addition, the drag coefficient profiles at various reduced frequencies have similar characteristics to the lift coefficient profiles, but the magnitude of drag increment is only small values. However, the profiles of the pitching-moment coefficient of the EOS show an opposite characteristic to that with the lift coefficient profiles. The pitching-moment coefficient becomes less negative with increasing the amplitude of the stage separation until the subsequent steps of the amplitude, when the gradient of pitching-moment coefficient changes. In the gap region, as shown in Figs. 9 and 10, increasing amplitude of the orbital stage at the beginning separation results in, respectively, lower flow density and higher flow velocity from expansion waves generated by the cavity of the ELAC configuration. As a result, both stages undergo a flow suction in the gap region (hence, the decreased lift coefficient and less-negative pitching-moment coefficient of the orbital stage). A further increase in amplitude at the larger gap of the unsteady flow may have reciprocal effects on expansion waves, causing a decrease in flow velocity in the gap region and an increase in static pressure of the orbital stage. As a result, the lift coefficient increases and the pitching-moment coefficient returns to a higher negative value.

B. Instantaneous Flow Features of Stage Separation

Figures 9 and 10 show the images of instantaneous density and Mach number contours at the reduced frequency of 1.0 for the continuous orbital motion at the beginning separation. This is the simulation of the fastest separation maneuver, in which the required time for staging from the lower condition to the upper condition is 0.065 s.

At the time of 0.0 s, for which the separation distance is 0.125 and the orbital angle of attack is 2.0 deg, the density contours at the symmetry plane in Fig. 9 indicate that the bow shock wave of the ELAC impinges on the bow shock of the EOS close to the EOS nose. By increasing the separation time, the bow shock wave of the ELAC moves from the upper bow shock wave part to the lower bow shock wave part of EOS, corresponding to the motion of EOS. Before affecting the EOS bow shock, the line of the ELAC bow shock bends, due to the induced vertical velocity flow. The bow shock wave of the EOS spreads out downstream, but in the symmetry plane, this effect can only be seen above and below the EOS surface. The upper bow shock angle seems to increase when it is closer to the maximum amplitude.

In the gap region, the flow on the upper surface of the ELAC experiences an expansion through the beginning of the curvature of the cavity (used to integrate the orbital-stage EOS in the first flight plane) and forms an expansion wave in the flow region between the ELAC and EOS stages. In the cavity, the flow also exhibits a shock wave, due to the curved surface downstream. This shock wave spread out in the same region. Both the cavity expansion and shock waves interact with the lower part of the extended bow shock of the EOS occurring in the middle flow region between both stages. The shock wave emanating from the cavity propagates farther and hits the rear part of the lower surface of the EOS on which it is reflected. With increasing amplitudes of the EOS stage, the location of the interaction points of the bow shock waves, expansion waves, and reflected shock waves move further downstream.

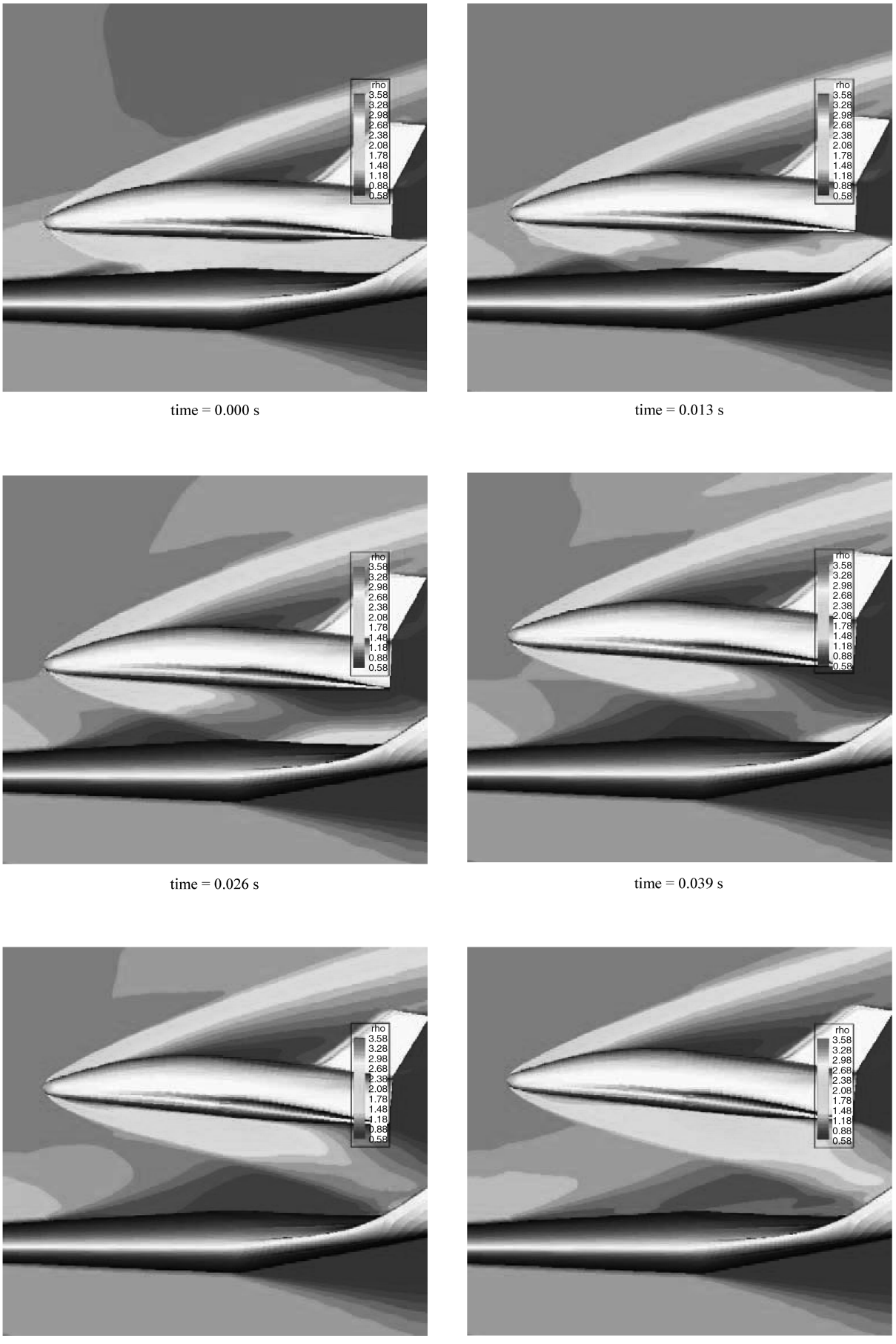

Fig. 9 Instantaneous density contours at six different time levels during separation at $M_\infty = 4.04$, $\alpha = 0.0\,\text{deg}$, $\Delta\alpha = 2.0\text{–}6.0\,\text{deg}$, $h/l_{\text{EOS}} = 0.125 - 0.325$, and $k_{\text{red}} = 1.00$.

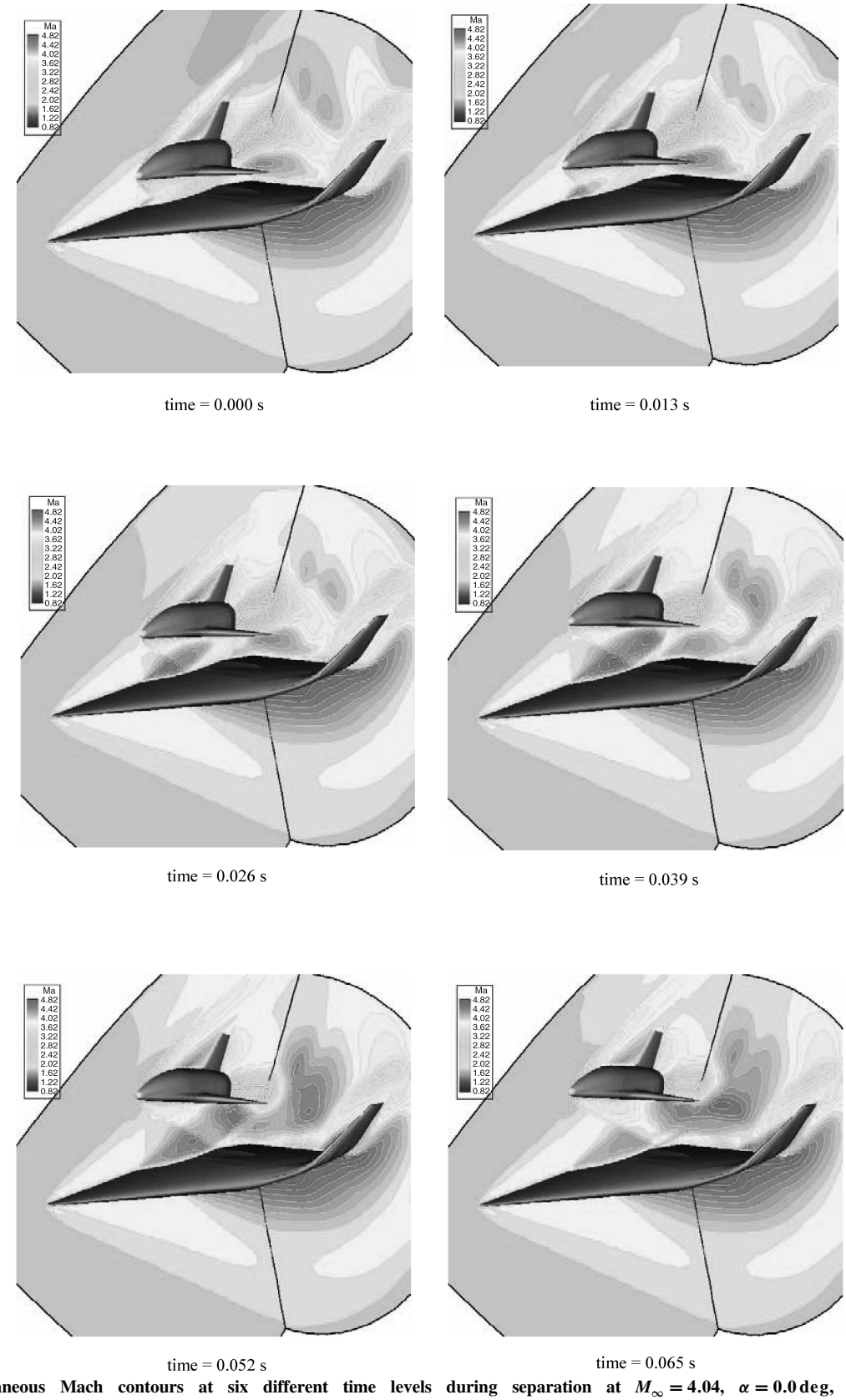

Fig. 10 Instantaneous Mach contours at six different time levels during separation at $M_\infty = 4.04$, $\alpha = 0.0\,\text{deg}$, $\Delta\alpha = 2.0$–$6.0\,\text{deg}$, $h/l_{\text{EOS}} = 0.125 - 0.325$, and $k_{\text{red}} = 1.00$.

The 3-D Mach number contours at a reduced frequency of 1.0, as shown in Fig. 10, show an increasing effect of the unsteady flow on the flowfield. Such an unsteady flow at the lower amplitudes obtains a lower Mach number flow; hence, the higher lift coefficient of the EOS results. However, an increase in the amplitude of the separation provides the higher Mach number flow or higher suction flow in the gap region, so that the EOS vehicle is subjected to a large decrease in the lift coefficient. With the subsequent increase in amplitude to the end position, the Mach number generated by the expansion wave from the cavity of the ELAC vehicle slightly decreases.

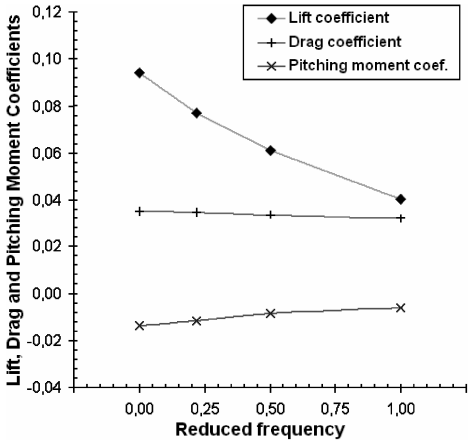

Fig. 11 Comparison of aerodynamic characteristics of steady and unsteady flows for various reduced frequencies at $M_\infty = 4.04$, $\alpha = 0.0$ deg, $\Delta\alpha = 4.0$ deg, and $h/l_{\text{EOS}} = 0.225$.

C. Comparison Between the Unsteady- and Steady-State Solutions

Figure 11 shows the comparison of aerodynamic characteristics for the steady-flow and unsteady-flow solutions at various reduced frequencies with a freestream Mach number $M_\infty = 4.04$, ELAC angle of attack $\alpha = 0.0$ deg, orbital-stage angle of attack $\Delta\alpha = 4.0$ deg, and separation distance $h/l_{\text{EOS}} = 0.225$. The reduced frequency equal to zero indicates that the flow is in a steady-flow condition. The unsteady aerodynamic characteristics are computed for the continuous orbital motion.

Increasing the reduced frequency provides the decreased lift coefficient of the EOS at the middle position of the separation. Compared with the steady-flow solution, the lift coefficient at the highest reduced frequency (namely, $k_{\text{red}} = 1.0$) decreases from 0.1 to 0.039. At the higher reduced frequencies, the decrease of the EOS lift during the separation maneuver should be taken into account. In addition, the drag coefficients of the EOS at various reduced frequencies are almost the same as the drag coefficient of the steady-state solution. This means that the downwash has only a slight effect on the drag coefficient. Also, increasing the reduced frequency of the

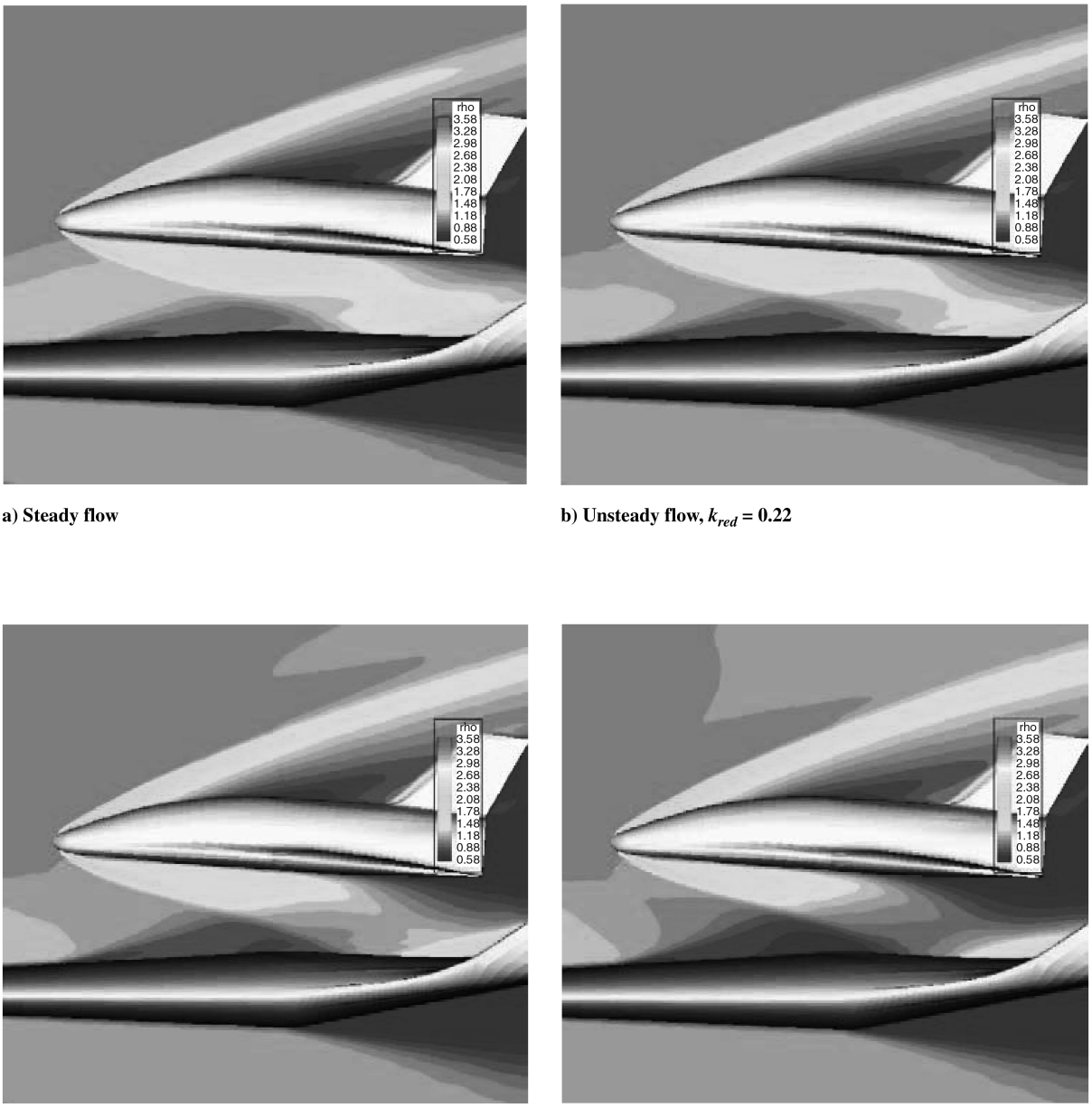

a) Steady flow

b) Unsteady flow, $k_{red} = 0.22$

c) Unsteady flow, $k_{red} = 0.50$

c) Unsteady flow, $k_{red} = 1.0$

Fig. 12 Comparison of density contours of steady and unsteady flows for various reduced frequencies at $M_\infty = 4.04$, $\alpha = 0.0$ deg, $\Delta\alpha = 4.0$ deg, and $h/l_{\text{EOS}} = 0.225$.

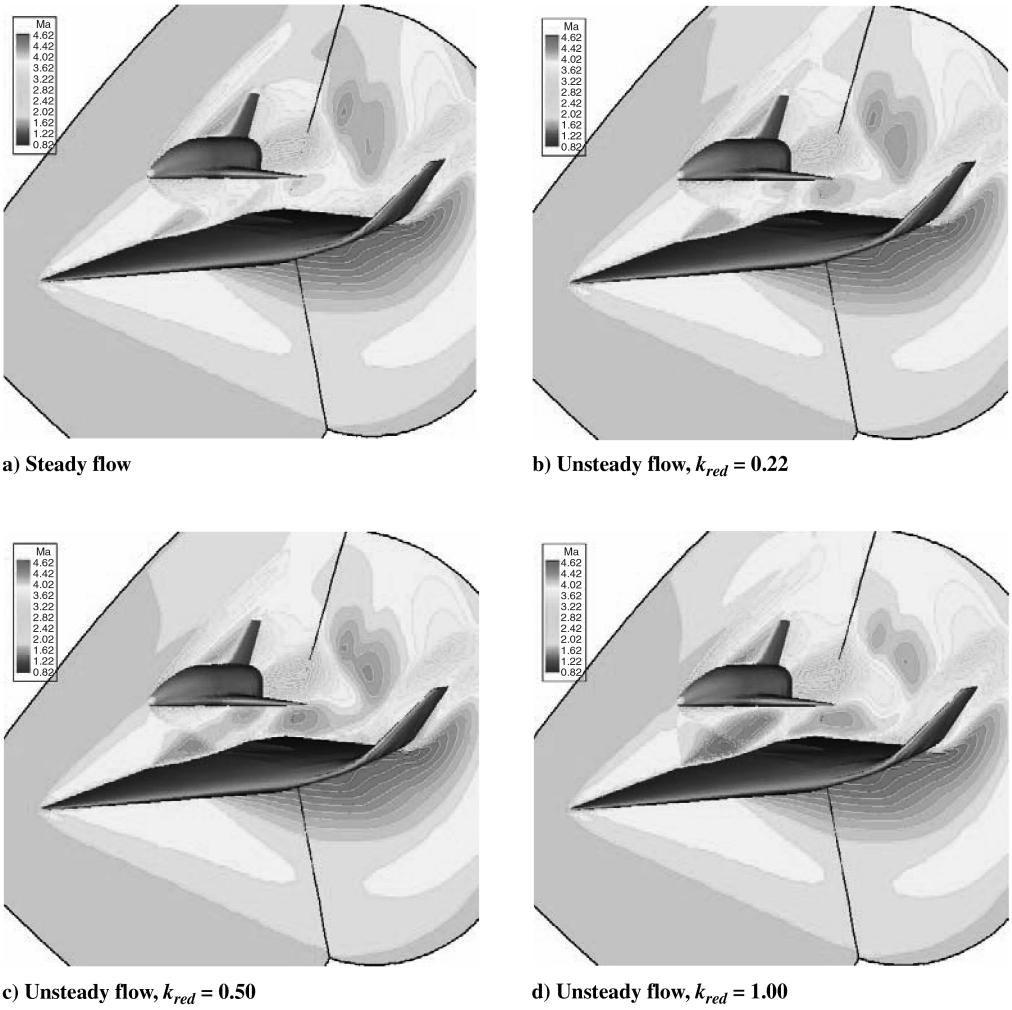

a) Steady flow **b) Unsteady flow, k_{red} = 0.22**

c) Unsteady flow, k_{red} = 0.50 **d) Unsteady flow, k_{red} = 1.00**

Fig. 13 Comparison of Mach contours of steady and unsteady flows for various reduced frequencies at $M_\infty = 4.04$, $\alpha = 0.0\,\text{deg}$, $\Delta\alpha = 4.0\,\text{deg}$, and $h/l_{\text{EOS}} = 0.225$.

EOS yields the significant decrease in the magnitude of the pitching moment.

Figures 12 and 13 show the density and Mach number contours for the steady and unsteady cases at various reduced frequencies: namely, $k_{\text{red}} = 0.22$, 0.5, and 1.0, respectively. Compared with the steady solution, the effect of the unsteady flow is clearly indicated by the bending line of the bow shock wave. It also affects flow features in the region above the EOS and in the gap region in Fig. 12. The effect of the unsteady flow provides an increase of flow speed in the gap region, as shown in Fig. 13, which causes a suction effect on both vehicle stages. However, the effect of induced flow does not have a significant impact to the flow under the ELAC vehicle.

Figures 14–16 show the graphs of lift, drag, and pitching-moment coefficients versus amplitude, respectively. The amplitude includes the orbital-stage angle of attack and separation distance between the stages, which change simultaneously. The unsteady results are computed for the case of the continuous orbital motion at the beginning separation, which is obtained from the computations at the second cycle. The results of the aerodynamic characteristics at the steady-state condition for three different positions (including the lower, middle, and upper positions) are also presented in the figures. Compared with the steady-state solution, at the lower position, the effect of the unsteady flow provides the additional lift of the EOS. This is caused by the time-dependent flows inducing a deceleration of the flow in the gap region, as shown in Fig. 10. But at the moderate and higher amplitudes, the unsteady flows cause a decrease in lift coefficient of the EOS. This may be due to the unsteady flow at the larger gap providing reciprocal effects on expansion waves generated by the cavity of the ELAC vehicle. In addition, the lift coefficient at the lower reduced frequencies is closer to the steady-state solution.

Subsequently, Fig. 15 shows that the unsteady drag coefficient at the same reduced frequency has a trend similar to the unsteady lift coefficient. The vehicle drag is mainly contributed by shock waves occurring in the flowfield. At the lower position, the unsteady-flow effect contributes a small additional drag coefficient. The extra drag coefficient becomes higher with increasing the reduced frequency.

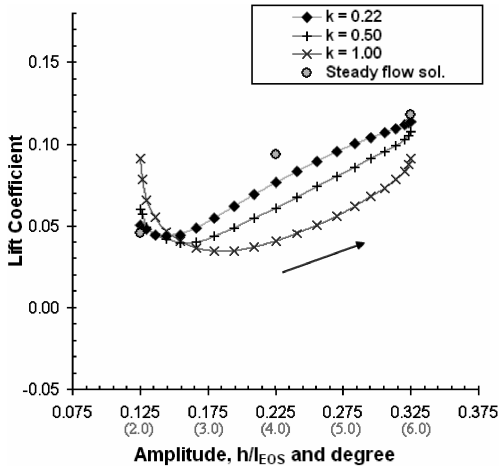

Fig. 14 Graphs of lift coefficient versus amplitude for various reduced frequencies at $M_\infty = 4.04$ and $\alpha = 0.0\,\text{deg}$.

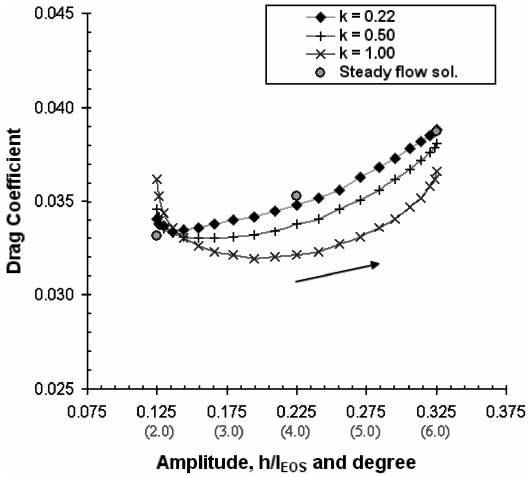

Fig. 15 Graphs of drag coefficient versus amplitude for various reduced frequencies at $M_\infty = 4.04$ and $\alpha = 0.0$ deg.

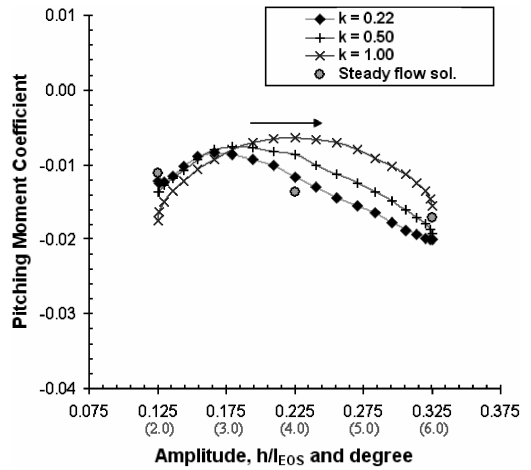

Fig. 16 Graphs of pitching-moment coefficient versus amplitude for various reduced frequencies at $M_\infty = 4.04$ and $\alpha = 0.0$ deg.

However, at the moderate and higher amplitudes, the unsteady flow causes a decrease in the drag coefficient. This is because the contribution of the expansion wave generated by the cavity of the ELAC vehicle increases and the reflected shock wave decreases. The subsequent increase in amplitude causes the increased effect of the bow shock of the EOS, and hence the drag increases again, as shown in Fig. 15. In addition, the drag coefficient for the lower reduced frequencies is closer to the steady-state solution.

Figure 16 shows the comparison of the steady and unsteady pitching-moment coefficients. The values of the pitching-moment coefficients for all amplitudes of the separation are negative. The pitching-moment coefficient becomes less negative with increased amplitude; before reaching the middle position, the pitching-moment coefficient becomes more negative with a further increase in the amplitude. At the lower position, the effect of the unsteady flow causes the EOS pitching-moment coefficient to become more negative. At a higher reduced frequency, the negative value of the pitching moment of EOS increases in magnitude, whereas the pitching-moment coefficient becomes less negative, due to the unsteady-flow contribution at the moderate and higher amplitudes.

IV. Conclusions

Unsteady aerodynamic investigations on stage separation of a TSTO space transportation system were performed based on the computational method. The investigations were accomplished for the complete geometry, consisting of a carrier stage (ELAC) and an orbital stage (EOS). The simulations of the stage separation were carried out by an upward movement of the orbital stage, relative to the carrier stage from the beginning separation, to a position at which no interaction occurred between stages. The motion of the orbital stage causes a downwash, changing with time and with the changes of the position and intensity of shock waves and the points of interaction of the reflected shock waves. This provides characteristics different from those with the steady-state computation discussed in part 1, for which the orbital stage is set at the fixed positions relative to the carrier stage without any change in flowfield with time. From the steady-state results, lift and drag coefficients of the orbital stage increase linearly with increasing the position of the separation. But the pitching moment decreases linearly to negative values with increasing the distance of the orbital stage relative to the carrier stage. For the unsteady-flow condition, the separation process affects lower lift and drag coefficients of the orbital stage, except for the beginning separation, and slightly increases in amplitude of the orbital stage from the beginning position, compared with the corresponding steady-state result. On the contrary, at the same conditions, the separation causes more positive pitching moment of the orbital stage than with the steady-state results.

The amount of reduced frequency determines the time rate of separation of the orbital stage, which influences the flow behavior and aerodynamic characteristics of the vehicle system. At the beginning separation, increasing the reduced frequency results in a higher speed of separation, which causes a higher additional lift and drag of the orbital stage referring to the steady-state result, whereas the pitching moment of the orbital stage becomes more negative with increasing the reduced frequency. Through the increase in amplitude of the orbital stage, the reduction rate of lift and drag increases with increasing the reduced frequency. In addition, the higher reduced frequency produces a higher increment rate of pitching moment. This requires a careful consideration of operation vehicle system at a higher reduced frequency, starting from the beginning separation at the position close to the carrier stage, when the orbital stage experiences a large lift reduction with increasing amplitude. At the same time, the pitching-moment coefficient of the orbital stage remains less negative at the beginning separation.

For future research, further investigation of the separation process of the space transport system considers a supporting mechanism to elevate the orbital stage from a position closer to the carrier stage to a final position of the mechanism. In addition, when the distance between the orbital and carrier stages is small, the viscous effects in the gap region cannot be ignored.

Acknowledgment

This research was supported by Deutsche Forschungsgemeinschaft (DFG) through the Collaborative Research Center 255 program, "Transatmospheric Flight Systems—Fundamentals of Aerothermodynamics, Propulsions and Flight Mechanics," at the Technische Universität München.

References

[1] Breitsamter, C., Jiang, L., and Moelyadi, M. A., "Stage Separation—Aerodynamics and Flow Physics," *Basic Research and Technologies for Two-Stage-to-Orbit Vehicles*, Deutsche Forschungsgemeinschaft, Bonn, Germany, and Wiley-VCH, Weinheim, Germany, 2005, pp. 101–124.

[2] Decker, J. P., "Aerodynamic Interference Effects Caused by Parallel-Staged Simple Configurations at Mach Numbers of 3 and 6," NASA TN D-5379, 1969.

[3] Bernot, P. T., "Abort Separation Study of a Shuttle Orbiter and External Tank at Hypersonic Speed," NASA TM X-3212, 1975.

[4] Bonnefond, T., Adamov, N. P., Brodetsky, M. D., Vasenyov, L. G., Derunov, E. K., and Kharitonov, A. M., "An Experimental Investigation of Aerodynamic Interference of TSTO Winged Systems During Separation," *Thermophysics and Aeromechanics*, Vol. 3, No. 4, 1996, pp. 285–292.

[5] Bonnefond, T., Adamov, N. P., Brodetsky, M. D., Vasenyov, L. G., Derunov, E. K., and Kharitonov, A. M., "Separation of Winged Vehicles in Supersonic," 6th International Aerospace Planes and Hypersonic Technologies Conference, AIAA Paper 95-6092, 1995.

[6] Kharitonov, A., Brodetsky, M., Vasenyov, L., Adamov, L., Breitsamter, C., and Heller, M. "Investigation of Aerodynamic Characteristics of the Models of a Two-Stage Aerospace System During Separation," Inst. of Theoretical and Applied Mechanics, Novosibirsk, Russia, and Technische Univ. München, Munich, 2000.

[7] Glößner, C., "Druck und Wärmestromverteilung und Aerodynamische Beiwerte Auftriebsgestützter Wiedereintrittskörper," *Arbeits und Ergebnisbericht, Sonderforschungsbereich 253*, Rheinisch-Westfälische Technische Hochschule Aachen, Aachen, Germany, 2001.

[8] Mukovozov, M. V., "Method for Determining Interference Components of Aerodynamic Characteristics of Aircrafts Integrated with a Body of Revolution at Mach 3 and 6," *Applied Problem of Aeromechanics and Geo-Cosmic Physics*, Moscow Inst. of Physics and Technology, Moscow, 1990, pp. 73–80.

[9] Weiland, C., "Stage Separation Aerodynamics, Aerothermodynamics and Propulsion Integration for Hypersonic Vehicles," AGARD, Rept. R-813, Neuilly-sur-Seine, France, 1996, pp. 11.1–27.

[10] Schröder, W., Behr, R., and Menne, S., "Analysis of Hypersonic Flows Around Space Transportation System via CFD Methods," AIAA Paper 93-5067, 1993.

[11] Brenner, P., "Numerical Simulation of Three Dimensional and Unsteady Aerodynamics About Bodies in Relative Motion Applied to a SSTO Separation," AIAA Paper 93-5142, 1993.

[12] Rochholz, H., Huber, T., and Matyas, F., "Unsteady Airloads During Separation of an Idealized Two-Stage Hypersonic Vehicle," *Zeitschrift für Flugwissenschaften und Weltraumforschung*, Vol. 19, No. 1, 1995, pp. 2–9.

[13] Meakin, R., and Suhs, N., "Unsteady Aerodynamic Simulation of Multiple Bodies in Relative Motion," AIAA Paper 89-1996, 1989.

[14] Cvrlje, T., Breitsamter, C., and Laschka, B., "Unsteady and Coupling Aerodynamic Effects on the Lateral Motion in Hypersonic Flight," 9th International Space Planes and Hypersonic Systems and Technologies Conference, AIAA Paper 99-4832, 1999.

[15] Cvrlje, T., Breitsamter, C., Weishäupl, C., and Laschka, B., "Euler and Navier–Stokes Simulations of Two-Stage Hypersonic Vehicle Longitudinal Motions," *Journal of Spacecraft and Rockets*, Vol. 37, No. 2, 2000, pp. 242–251. doi:10.2514/2.3552

[16] Decker, K., and Laschka, B., "Unsteady Aerodynamics of a Hypersonic Vehicle During a Separation Phase," AIAA Paper 2001-1852, 2001.

[17] Jameson, A., "Time Dependent Calculations Using Multigrid, with Applications to Unsteady Flow Past Airfoils and Wings," AIAA Paper 91-1596, 1991.

[18] Guillard, H., and Farhat, C., "On the Significance of the GCL for Flow Computations on Moving Meshes," AIAA Paper 99-0793, 1999.

[19] Jameson, A., Schmidt, W., and Turkel, E., "Numerical Simulation of the Euler Equation by Finite Volume Methods Using Runge–Kutta Time Stepping Schemes," AIAA Paper 81-1259, 1981.

[20] Sachs, G., Drexler, J., and Schoder, W., *Optimal Separation and Ascent of Lifting Upper Stages*, Lecture Notes in Engineering, Springer–Verlag, Berlin, 1993, pp. 325–331.

[21] Laschka, B., "Grundlagen der Stationären und Instationären Strömungen," *Vorlesungsmanuskript*, Inst. for Fluid Mechanics, Technische Univ. Munchen, Garching, Germany, 1999.

R. Cummings
Associate Editor